1

Spectroscopic Characterization of Graphitic Nanomaterials and Metal Oxides for Gas Sensing

Olasunbo Farinre, Hawazin Alghamdi, and Prabhakar Misra

Howard University, Department of Physics and Astronomy, Laser Spectroscopy Laboratory, 2355 6th St., NW, Washington, DC 20059, USA

1.1 Introduction and Overview

1.1.1 Graphitic Nanomaterials

Environmental pollution is a growing global concern due to its negative impact on human health, and on the Earth's climate system caused by global warming. In this context, it is important to monitor pollutants and therefore there is an increased need for gas sensors with useful properties, such as high sensitivity and selectivity for identification, monitoring, and removal of toxic gases from the environment. In principle, gas sensors are devices that detect the type, components, and concentration of a target gas and in turn provide electrical and/or optical signals for quantifying the output following successful detection. Gas sensors are not only useful for environmental monitoring of toxic gases but are equally applicable for detecting explosives and flammable gases for military applications. Gas sensors can be classified into various categories, especially based on their responses to effects of humidity, and they include field effect transistor (FET)-based sensors (see Figure 1.1), optical fiber sensors (OFS), and chemiresistors. Chemiresistors are the most widely used type of gas sensors because they are cost-effective, are easy to operate and have low power consumption [1]. Chemiresistors work on the principle that gas molecules adsorbed on the sensitive layer changes its electrical resistance. A quality gas sensor should have the following properties: (i) high sensitivity for the target molecules being sensed; (ii) high selectivity to differentiate various gas species, when multiple gases are being sensed; (iii) high stability to give accurate output over long periods of time; (iv) consistency in test results when gas sensors are tested under similar conditions; and (v) low detection limit and ability to operate optimally at room temperature [2]. Various nanomaterials, such as conducting polymer nanowires (polyaniline [PANI], polypyrrole), metal oxide semiconductors, and atomically thin transition metal dichalcogenides, have been extensively studied and widely used as gas-sensing materials. For example, earlier research studies have reported that gas sensors fabricated from PANI nanowires are cost-effective and have

Spectroscopy and Characterization of Nanomaterials and Novel Materials: Experiments, Modeling, Simulations, and Applications, First Edition. Edited by Prabhakar Misra.

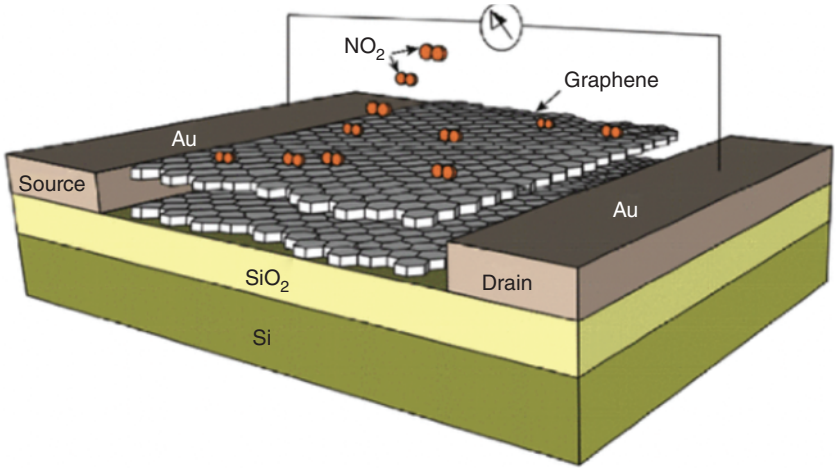

Figure 1.1 Field effect transistor (FET) graphene-based gas sensor for NO_2 detection. Source: Copyright ©2016, Wang et al. [16]) https://creativecommons.org/licenses/by/4.0/.

good sensitivity and fast response time due to their high surface area and are operable at room temperature [3, 4]. However, in neutral and high pH environments, the PANI nanowire-based gas sensors exhibit slow response time and loss of conductivity and have short life spans, thereby making them unattractive for sensing gas analytes [4, 5]. Overall, metal oxide semiconductors can be good gas-sensing materials due to their low cost, ease of fabrication, and high sensitivity; however, some of its major drawbacks are the need for higher temperatures for their operability, poor selectivity, and short life span [1, 6–8].

The unique morphology of graphitic nanomaterials, such as carbon nanotubes (CNTs), graphene, and graphene nanoplatelets (GnPs), and their fascinating electrical, thermal, and mechanical properties make them more appealing gas-sensing materials as compared to the traditional metal oxide semiconductors. Effort has been directed toward investigating graphitic nanomaterials and composites-based gas sensors, leading to a significant leap in the development of gas-sensing devices based on these materials [3, 6, 9]–[12]. Graphene is a two-dimensional (2D) material that has become the subject of major scientific interest for researchers since its discovery in 2004 by Geim and Novoselov [13]. This is due to its outstanding morphological, mechanical, and electronic properties, and its high surface area to volume ratio that enhances the adsorption of target molecules and enables modification of its surface by various functional groups, which make functionalized graphene particularly attractive as a good sensing material [6, 14, 15]. Graphene has a honeycomb structure where the carbon atoms are arranged in a hexagonal ring with an atomic separation of 1.42 Å. Each carbon atom is linked to three neighboring carbon atoms via three σ bonds and one π-bond. The hybridization of 2s and 2p atomic orbitals of neighboring carbon atoms form the σ covalent bonds, while the p_z orbitals form the π-bond.

CNTs, which are one-dimensional (1D) nanostructures were re-discovered in 1991 by Sumio Iijima [17], which in turn paved the way for the emergence of other

nanomaterials. Since their discovery, CNTs have been studied extensively for a range of applications, including energy storage, nanoprobes, drug delivery, and electronics, due to their excellent electrical and thermal conductivity, and high mechanical strength [18]. CNTs are good candidates for applications in gas sensing, because they are cheap and have low weight and because of their morphology (high aspect ratio), making them well suited for gas adsorption [19, 20]. CNTs can be categorized into two types based on the number of wall layers: single-walled carbon nanotubes (SWCNTs) and multiwalled carbon nanotubes (MWCNTs). SWCNTs are formed when single-layer graphene is rolled into a cylinder having a diameter of approximately 0.4–2 nm [18], while the MWCNTs are formed when several graphene layers are rolled into concentric cylinders. CNTs can either be semiconducting or metallic based on their geometry (chirality vector (n, m)). CNTs with armchair configuration ($n = m$) are metals, while those with chirality $n - m = 3j$, where j is a nonzero integer are quasi-metallic and the rest are moderately semiconducting [19].

GnPs are derivatives of graphene and graphite because they are manufactured from the exfoliation of graphite. Hence, GnPs have potential applications in gas sensing because of their lightweight, large surface-area-to-volume ratio, high thermal conductivity and stability, and superior mechanical rigidity. In addition, GnPs can be produced on a large scale and have a well-established growth and fabrication process [21]. The honeycomb structure possessed by GnPs is the same as in 2D graphene. Also, GnPs are similar to graphite in terms of the interlayer distance of approximately 3.35 Å, which can be determined using the X-ray diffraction (XRD) technique. GnPs appear in aggregates when viewed with an electron microscope, and these aggregates consist of sub-micron-sized platelets that are few nanometers thick. Each of these sub-micron platelets consists of small stacks of graphene sheets that typically range in thickness from about 0.34–100 nm [22].

1.1.1.1 Synthesis of Graphitic Nanomaterials

There are three primary techniques commonly used in producing CNTs in large quantities, namely chemical vapor deposition (CVD), laser vaporization (LV), and the arc discharge (AD) [23].

1. CVD Method: This is the most widely used method in producing CNTs commercially. In this method, a catalyst material that is present in a high-temperature chamber (at approximately 600–1200 °C) decomposes carbon containing vapor and induces growth of CNTs on the catalyst material (see Figure 1.2). Afterward, the CNTs are retrieved from the chamber, when it has cooled to room temperature, in order to avoid oxidation of the nanotubes [23].
2. LV Method: This technique involves the use of a laser to evaporate graphite in a high-temperature chamber. The nanotubes appear as the vaporized carbon condenses and are grown on the cooler surfaces of the reactor. CNTs produced using this technique are highly pure but cannot be mass-produced on a large scale [24].

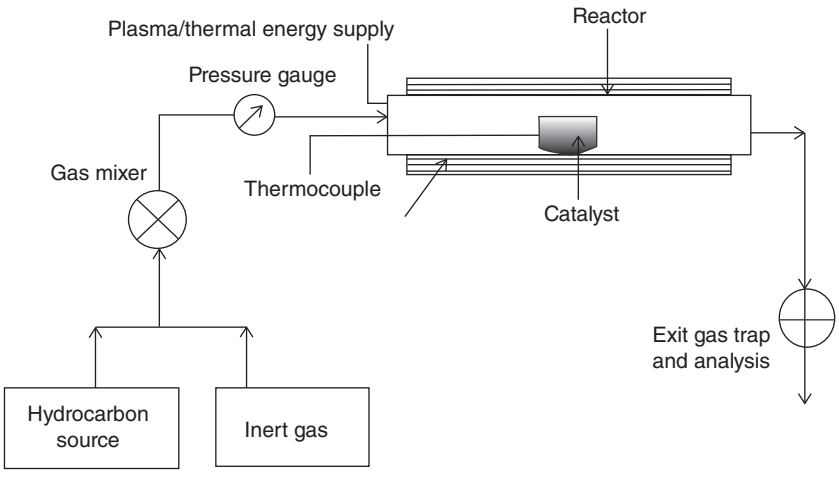

Figure 1.2 Schematic diagram of CVD synthesis of carbon nanotubes (CNTs). Source: Copyright ©2010, Mohamed et al. [25] https://creativecommons.org/licenses/by/4.0/.

3. AD Method: CNTs were experimentally discovered by this method in 1991 in the carbon-soot of graphite electrodes. In this technique, graphite electrodes are evaporated at very high temperatures in an electric arc to produce a carbon plasma [23, 24].

Graphene was isolated by Geim and Novoselov in 2004 in the form of small flakes through the micro-mechanical cleavage of graphite layers by using a scotch tape [13]. A variety of techniques employed to synthesize graphene have been developed, since the discovery of graphene and these include chemical exfoliation, CVD, reduction of graphene oxide (GO), and epitaxial thermal growth on a silicon carbide (SiC) surface. The CVD technique is widely used to synthesize single-layer graphene, especially for gas-sensing applications. The CVD technique involves the disintegration of gaseous hydrocarbon precursors in a high-temperature reaction chamber that are made to come into contact with a heated substrate within the chamber [26]. A reaction occurs and creates a material film in the form of single-layer graphene on the surface of a substrate, after which waste gases are pumped out of the reaction chamber (see Figure 1.3). Some common substrates used in the CVD process are nickel, copper, and platinum. The CVD technique is highly suitable for producing high purity graphene on a large scale. However, it involves a complex production process that is expensive and lacks ability to produce multiple graphene layers to order [6]. The chemical exfoliation method is another popular method that has been used extensively to synthesize single-layer graphene commercially. Sharma et al. [27] reported the chemical exfoliation of graphite by dispersing graphite in ortho-dichloro benzene (ODCB) solvent and sonicated to form a homogeneous mixture of single-layer graphene. The homogeneous mixture was then appropriately centrifuged to remove unexfoliated graphite aggregates, subjected to high temperature, and later dried in the oven prior to being deposited on a silicon wafer substrate. This particular technique has been universally adopted in the production of

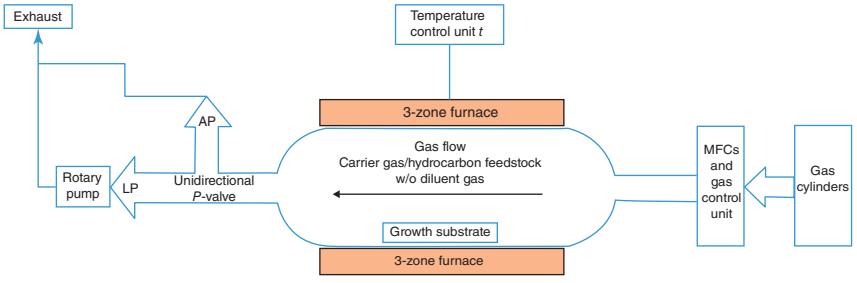

Figure 1.3 Schematic diagram showing a hot-wall horizontal tube-furnace CVD system (LP, low pressure; AP, atmospheric pressure). Source: Copyright ©2020, Multidisciplinary Digital Publishing Institute. Saeed et al., [30] https://creativecommons.org/licenses/by/4.0/.

graphene commercially because it is cost-effective and suitable for producing single- and few-layer graphene at high concentration [28]. Mechanical exfoliation was a pioneering technique employed by Geim and Novoselov in 2004 [13] to synthesize single-layer graphene using a scotch tape. The scotch tape was placed directly on the surface of highly ordered pyrolytic graphite (HOPG) and pulled up to exfoliate few layers of graphene; the process was then repeated until a single layer of graphene was left on the tape, after which the tape was dissolved and the single-layer graphene transferred to a substrate [15]. Pirzado et al. [29] reported the synthesis of few-layer graphene (FLG) through the mechanical exfoliation of graphite disk on a glass substrate, which was subsequently pulled up from the glass substrate using ethanol by forming a suspension. The sedimentation process separated FLG in liquid form from the suspension and oven-dried in vacuum at 100 °C. The FLG films were eventually transferred to a heated quartz substrate and dried again. The mechanical exfoliation technique is an inexpensive technique that can be used to produce graphene but cannot be used to mass-produce graphene commercially.

The methods used in the exfoliation of graphite into single- or few-layered GnPs vary, but one of the most commonly used method involves liquid-phase exfoliation (see Figure 1.4). Other techniques which have been recently employed in synthesizing GnPs are shear mixing and wet-jet milling. These processes are employed in the large-scale production of high-quality GnPs. Ding et al. [31] reported the use of an eco-friendly liquid-phase exfoliation process to exfoliate graphite layer by layer in order to produce GnPs in degassed pure water. Firstly, graphite powder is dispersed in distilled water and a homogenous mixture is formed by sonication. During the exfoliation process, the sonicated mixture is subjected to high-temperature vapor, which in turn breaks the van der Waals forces between the layers and leads to a separation of the graphite layers and insertion of water molecules between the layers. Hydroxyl (–OH) and carboxyl (–COOH) groups were also added to the edges of the nanoplatelets [31]. The exfoliation process usually introduces naturally occurring functional groups to the edges of the nanoplatelets. The chemical reactivity of the carbon atoms localized at the edges of GnPs makes it possible to functionalize GnPs at the edges. Functionalized GnPs can be produced using a dielectric barrier discharge (DBD) plasma process under atmospheric pressure. The main goal of plasma

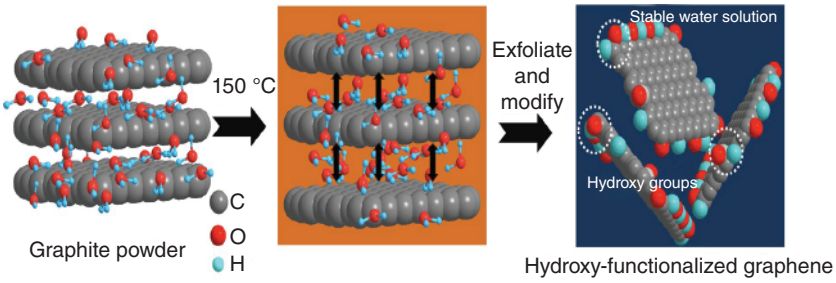

Figure 1.4 Schematic illustration of liquid-phase exfoliation process of graphite. Source: Copyright ©2018, Nature Publishing Group, Ding et al. [31]. https://creativecommons.org/licenses/by/4.0/.

functionalization is to provide a greater control over the desired type and extent of functionality to be introduced in the nanoplatelets. The plasma functionalization of GnPs with specific functional groups are realized using monomer gases carrying the desired functional group, where the monomers used include the amino, hydroxyl, and carboxyl groups. One of the major purposes of functionalizing exfoliated GnPs is to control the hydrophilicity of GnPs for easier dispersion in polymers and resins. The DBD plasma method is the most commonly used method for functionalization because it is inexpensive, fast, clean, and easily controllable [32].

1.1.2 Metal Oxides

Metal oxides have found utility in a variety of different fields. For instance, they have been incorporated in research related to material science, geology, mechanical and electrical engineering, condensed matter physics, and inorganic chemistry. Such oxides have been utilized in a variety of applications, such as catalysis, medicine (e.g. biosensor technology), environmental monitoring (e.g. water treatment, reduction of air pollutants, and purification of industrial waste outcome), and optronics [33, 34]. A number of semiconducting metal oxides, such as SnO_2, TiO_2, ZnO, NiO_2, etc., have been used in energy storage and solar cell applications. Specifically, tin dioxide (SnO_2) has been investigated for use in a wide variety of applications. It has been tested in solar cells as an anti-reflection coating and as a solar energy absorption coating, in rechargeable lithium-ion batteries, and most commonly in gas-sensing devices [35]. Transparent conducting oxides (TCOs) have been the center of attention in the past 20 years (e.g. SnO_2, In_2O_3, CdO, Ga_2O_3, ZnO, etc.) due to their interesting properties. These oxides have found applications in high-resolution displays and screens (i.e. liquid crystal displays [LCDs], high-definition televisions [HDTVs], organic light-emitting diodes [OLEDs]), portable smart devices, smart windows, and thin film photovoltaics [36]. One particular TCO material, SnO_2, exhibits large optical transparency and small electrical resistance. Even though, SnO_2 is transparent in the visible region of the electromagnetic spectrum, it still has large reflectivity in infrared (IR) light. Therefore, both SnO_2 and fluorine doped (SnO_2/F) are commonly applied as coating materials in energy-saving windows where they are effective in

limiting loss of radiative heat due to the small thermal emission around 0.15 in comparison to 0.84 for uncoated glass [37].

Tin (Sn) is a well-known posttransition metallic element that is located between transition metals and metalloids. When oxidizing Sn, it creates different heterovalent and univalent oxides, as for example SnO, SnO_2, Sn_2O_3, and Sn_3O_4. Each of them has unique chemical and physical properties and structures. Two of them (SnO and SnO_2) are most frequently studied due to their interesting applications and properties. The majority of prior studies have mainly concentrated on tin dioxide (SnO_2) and its different forms. SnO_2 is an n-type semiconductor material. It has a large direct band gap around 3.6 eV at room temperature, as a result of oxygen (O) vacancies and interstitial Sn atoms. SnO_2 has been recognized for its excellent conductivity due to elevated electron mobility, large transparency in visible light, and excellent chemical and thermal stability. SnO has garnered less attention, since it tends to be altered to SnO_2 under certain pressure and temperature conditions [38–41].

SnO_2 exists naturally in a tetragonal rutile structure, with a space group symmetry of $P4_2/mnm$. The rutile structure is considered essential and more stable in comparison to other structures of SnO_2. Different SnO_2 structures can be derived under certain mechanical pressure (e.g. $CaCl_2$-type [Pnnm], α-PbO_2-type [Pbcn]), fluorite-type [$Fm\bar{3}m$], pyrite-type [$Pa\bar{3}$], ZrO_2-type orthorhombic phase I [Pbca], and cotunnite-type orthorhombic phase II [Pnam]) [35]. SnO_2 has point symmetry of D_{4h}^{14} and space group symmetry of $P4_2/mnm$, with an electronic configuration of $4d^{10}\ 5s^2\ 5p^2$. SnO_2 has lattice constants $a = b = 4.7374$ Å and $c = 3.1864$ Å, where each unit cell contains two cation Sn^{4+} atoms and four anion O^{2-} atoms. Each Sn atom is located at the lattice vertices (i.e. $(0, 0, 0)$ and $(1/2a, -1/2a, 1/2c)$). The O atoms are connected to Sn atoms with a bond length of 2.057 Å to form an octahedral network, where the Sn atoms are situated in the interstitial sites of the O octahedral (i.e. $\pm(ua, -ua, 0)$ and $(1/2a, -1/2a, 1/2c)$, with $u = 0.307$). Two angles between equilateral O atoms α and β are shown in Figure 1.5, where the sum of these two angles is close to 180° (i.e. $\alpha = 78.1°$ and $\beta = 101°$) [42, 43]. This tetragonal structure of SnO_2 allows it to be anisotropic in manifestation of its optical and electronic properties. For instance, the shorter distance between Sn atoms along the *c*-axis may facilitate more conductive passage of electrons due to a higher orbital overlap in the crystal (see Figure 1.5) [36].

1.2 Spectroscopic Characterization of Graphitic Nanomaterials and Metal Oxides

1.2.1 Graphitic Nanomaterials

Prior to the fabrication process of graphitic nanomaterial-based gas sensors, it is important to gather relevant information with regard to their structural, chemical, and electronic configurations. Also, an accurate characterization of the surface chemistry and structure of graphitic nanomaterials is needed to study the changes that result from exposure to toxic gases. Experimental techniques, such as scanning

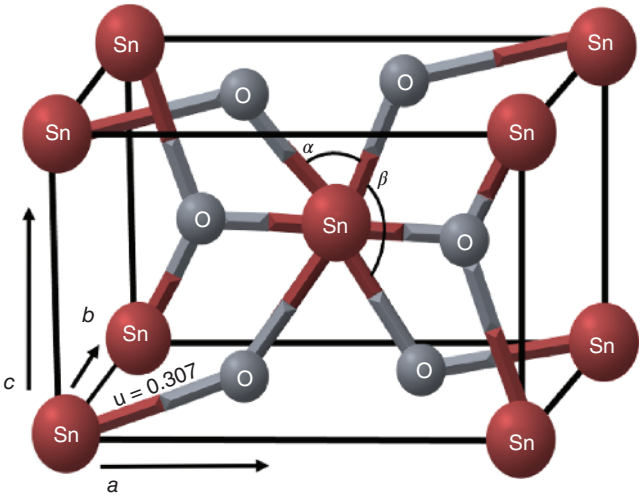

Figure 1.5 One-unit cell structure of SnO_2.

electron microscopy (SEM) and atomic force microscopy (AFM), give detailed information about the structural properties at the nanometer level, while Fourier transform infrared (FTIR) and Raman spectroscopy provide the vibrational properties, and the electronic information can be obtained via a DC measurement test of the nanomaterials. The present section gives a brief research overview of various analytical techniques that have been utilized to investigate the aforementioned properties of CNTs, graphene, and GnPs reported in the literature.

1.2.1.1 Characterization of Carbon Nanotubes (CNTs)

Raman spectroscopy is a spectroscopic tool that is commonly used for characterization of carbon-based materials because it requires minimal sample preparation, as compared to other techniques such as transmission electron microscopy (TEM) and AFM. Misra et al. [44] investigated the vibrational properties of SWCNTs utilizing Raman spectroscopy with a laser excitation wavelength of 780 nm. The 2D, G^+, G^-, and D peaks were recorded at frequencies 2580, 1594, 1565, 1294 cm^{-1}, respectively, and the radial breathing modes at frequencies 267.5, 234, and 206 cm^{-1} were observed in the Raman spectrum of SWCNTs (see Figure 1.6). Also, Misra et al. [44] reported the effects of increasing temperature over the range 27–200 °C on the Raman features of SWCNTs, which can provide insight into the response of CNT-based gas sensors at elevated temperatures. Their results showed that increasing the temperature shifts the 2D, G^+, G^-, D peaks and the radial modes of SWCNTs to lower frequencies. Furthermore, CNTs' surface can be functionalized either covalently or noncovalently to improve the adsorption of gas molecules on the surface, thereby improving the sensitivity and selectivity of CNT-based sensors. Botti et al. [45] investigated the vibrational properties of pristine and functionalized CNTs utilizing the surface-enhanced Raman spectroscopy (SERS) technique. This technique was chosen because it amplifies the Raman signal of the functional groups on the

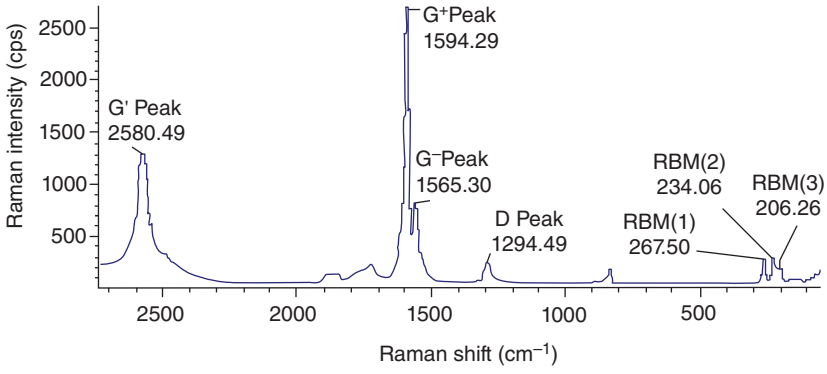

Figure 1.6 Raman spectrum of SWCNTs. Source: Copyright ©2014, Misra et al. [44]. https://creativecommons.org/licenses/by/4.0/.

surface of the CNTs by decreasing the distance between the CNTs and the adsorbed molecules. The SERS spectra of MWCNTs with increasing thickness were collected and Botti et al. [45] reported the main Raman features of CNTs to be the D, D′, G peaks, and the radial breathing modes. The SERS spectra of MWCNTs functionalized with carboxyl (COOH) and amino (NH_2) groups were also collected in the same study, and the results showed enhanced Raman peaks as compared to the conventional Raman spectra. Molecular vibrations attributed to C–O–C stretch (1260 cm^{-1}), C=O stretch (1730 cm^{-1}) in the Raman spectra of MWCNTs –COOH and molecular vibrations attributed to C–N stretch (1240, 1460 cm^{-1}) and C=O stretch (1730 cm^{-1}) in the Raman spectra of MWCNTs –NH_2 were also observed [45].

In another study, Misra et al. [46] utilized Raman spectroscopy, FTIR, and thermal gravimetric analysis to study the surface chemistry of nitrogen-doped MWCNTs. Thermal gravimetric analysis was carried out to measure the mass of nitrogen-doped MWCNTS in the temperature range 200–900 °C as a potential application in the removal of impurities and amorphous carbon from CNTs. The FTIR results showed the presence of Si–O, C–N, N–CH_3, C–O, and C–H peaks that appear at frequencies 1026, 1250, 1372, 2851, and 2925 cm^{-1}, respectively. The presence of the Si–O peak in the FTIR spectra was attributed to the presence of the silicon substrate on which MWCNTs were grown, while the presence of the C–N and N–CH_3 features was attributed to the presence of nitrogen atoms intercalated between the inner walls of the nanotubes and graphite layers. FTIR analysis was also carried out on MWCNTs after conducting thermal gravimetric analysis at 900 °C and the results showed that at this temperature the MWCNTs samples were completely destroyed following the removal of impurities in the temperature range 400–600 °C.

1.2.1.2 Characterization of Graphene and Graphene Nanoplatelets (GnPs)

Casimir et al. [47] investigated the vibrational properties of CVD graphene on a nickel substrate, HOPG and functionalized GnPs utilizing Raman spectroscopy with a 532-nm laser wavelength. Their results showed the presence of the G and 2D peaks at 1580 and 2700 cm^{-1}, respectively, in the Raman spectrum of graphene, which

exhibited greater intensity as compared to the G and 2D peaks of HOPG due to the presence of multiple graphene layers (see Figure 1.7). In addition, the authors reported the in-plane crystallite sizes of graphene, HOPG, and functionalized GnPs calculated from intensity ratios of the D and G peaks discovered by Tuinstra and Koenig [48] to be 71.8 nm, 1.3 μm, and 0.17 μm, respectively.

Another study by Thema et al. [49] in 2013 synthesized GO and reduced graphene oxide (RGO) from graphite powder and also investigated the structural, surface, and morphological properties using XRD, FTIR, Raman spectroscopy, and AFM techniques. FTIR was utilized to confirm the successful synthesis of GO and RGO. The XRD results confirmed the presence of intercalated oxygen functional groups in between the GO layers resulting in an interlayer distance of 0.76 nm. A broad peak at $2\theta = 25.80°$ in the XRD spectra of RGO indicated an interlayer distance of 0.34 nm signaling the removal of the intercalated oxygen atoms between the layers. The presence of a reduced peak indicating the presence of O–H stretching vibrations at 3400 cm^{-1}, C=O peak at 1720 cm^{-1}, and C–O peak at 1060 cm^{-1} were reported to be observed in the FTIR spectrum of RGO. Three-dimensional (3D) AFM topography images were generated for GO and RGO to indicate their levels of exfoliation and it was reported that the GO sheets were thicker due to the presence of oxygen functional groups and the sp^3-hybridized carbon atoms were displaced slightly toward the top and bottom of the exfoliated graphite plane. In addition, Thema et al. [49] reported a red-shift in the D and G bands of the Raman spectrum of RGO and the absence of the 2D band in the Raman spectrum of GO.

GnPs are also gaining enormous attention in recent times because of their potential applications in the next generation of sensor devices. Our research group, Farinre et al. [50] conducted a comprehensive study on the structural and vibrational properties of pristine and functionalized GnPs with carboxyl, fluorocarbon, nitrogen, oxygen, and ammonia and argon functional groups, utilizing Raman spectroscopy, XRD, and FTIR experimental techniques, along with Molecular Dynamics (MD) simulations. The Raman results showed an increase in the relative intensities of the D and G peaks (I_D/I_G) for functionalized GnPs due to the presence of functional groups in the structure, as compared to pristine GnPs and n-type doping character of GnPs functionalized with 35 wt% carboxyl group (see Figure 1.8).

Results from the XRD analysis were also reported and they showed that the functionalized GnPs have smaller crystallite sizes compared to pristine GnPs. Finally, MD simulation was carried out on pristine trilayer graphene, which closely matches the structure of the pristine GnPs samples, using the Large-scale Atomic/Molecular Massively Parallel Simulator (LAMMPS) software program – available from Sandia National Laboratories [51]. The results showed that the G, D, and 2D vibrational modes are in close agreement with the experimental results (see Figure 1.9).

1.2.2 Characterization of Tin Dioxide (SnO_2)

The majority of studies on tin dioxide focus on understanding the physical properties of the detecting material and finding ways to enhance their properties (i.e. selectivity and sensitivity) [34]. Even though metal oxides in general have large thermal

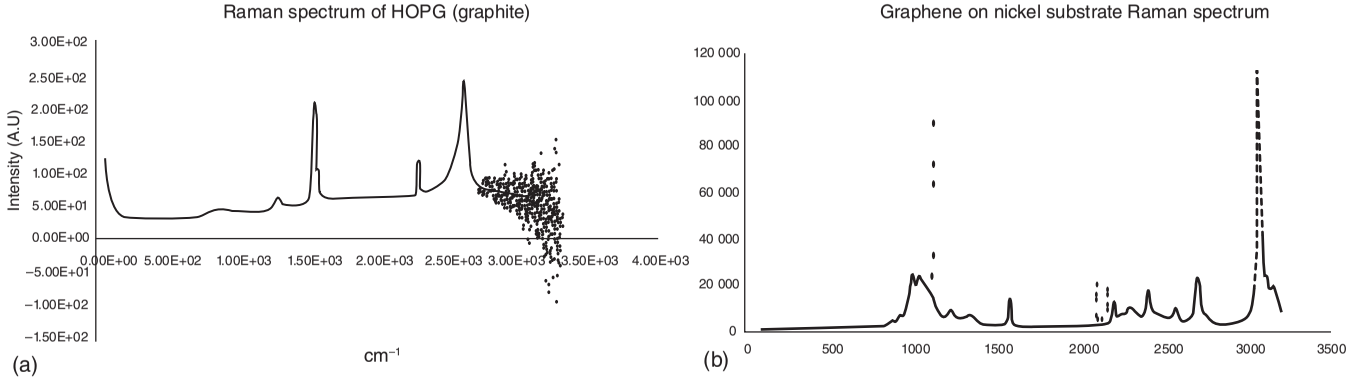

Figure 1.7 Raman spectrum of (a) highly ordered pyrolytic graphite (HOPG) and (b) graphene. Source: Copyright ©2019, Casimir et al. [47]. Available from DOI:10.5772/intechopen.84527.

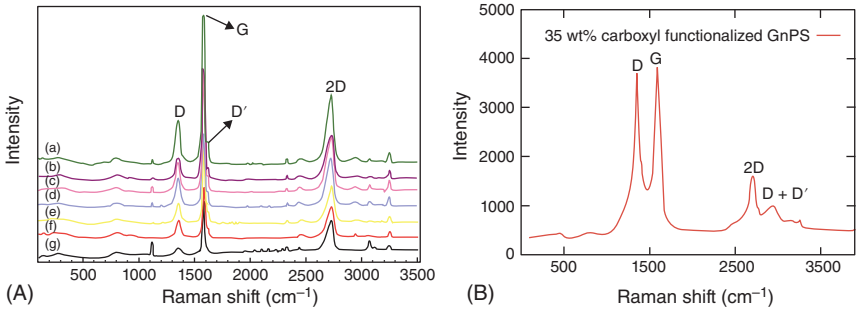

Figure 1.8 (A) Raman spectra of pristine and functionalized graphene nanoplatelets (GnPs) showing the vibrational modes: (a) carboxyl-GnPs, (b) fluorocarbon-GnPs, (c) nitrogen-GnPs, (d) ammonia-GnPs, (e) oxygen-GnPs, (f) argon-GnPs, and (g) pristine-GnPs; (B) Raman spectra of GnPs functionalized with 35 wt% of carboxyl.

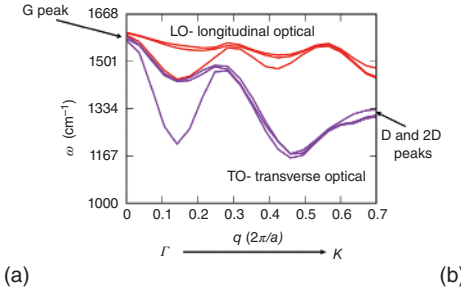

	Irreducible representation	ABC-trilayer (calculated)	Exp. data of GnPs (3–6 layers)
Γ	$E_{2g}(R)$	1581 cm^{-1}	1581 cm^{-1}(G peak)
	$E_{1u}(IR)$	1590 cm^{-1}	1670 cm^{-1}(C=C bond from IR spectra)
	$E_{2g}(R)$	1574 cm^{-1}	
K	$A_{1g}(R)$	1331 cm^{-1} (D peak) 2662 cm^{-1} (2D peak)	1353 cm^{-1} (D peak) 2722 cm^{-1} (2D peak)
	$E(R)$	1307 cm^{-1}	
	$E(R)$	1313 cm^{-1}	

(b)

Figure 1.9 (a) Phonon branches contributing to the D, G, and 2D Raman peaks; (b) Calculated and experimental values of Raman and infrared peaks.

stability, which allows them to last longer than other types of gas-sensing materials (e.g. metals, polymers, and organic semiconductors), metal oxide detectors are lacking in selectivity of target gases [52]. Therefore, it is important to characterize metal oxides – our focus is on studying SnO_2 properties in depth. The SnO_2 powder used in the spectroscopic characterization was commercially purchased with 325 mesh, 99.9% purity from (General Monitors, Lake Forest, CA). We have used XRD, which is a nondestructive and powerful method to characterize the crystal structure, orientation of SnO_2, and its crystallite size [41]. The XRD data of powdered SnO_2 have been collected for $2\theta = 20°–80°$. The diffraction angle values observed are associated with Miller Indices (*h k l*) at 26.34° (1 1 0), 33.60° (1 0 1), 38.25° (2 0 0), 51.56° (2 1 1), 55.01° (2 2 0), 62.13° (3 1 0), 64.97° (1 1 2), and 66.15° (3 0 1), respectively. Different faces of the SnO_2 crystalline structure are represented by each index, which verifies the rutile tetragonal structure with reference card number (JCPDS 41-1445), with no impurity features as shown in Figure 1.10 [53, 54].

The (1 1 0) plane denotes the lowest energy face of the SnO_2 single crystal, which constructs a larger portion of the surface area than presented by (1 0 1) and (1 0 0) with smaller faces [55]. Accordingly, we calculate the crystallite size (D) by applying

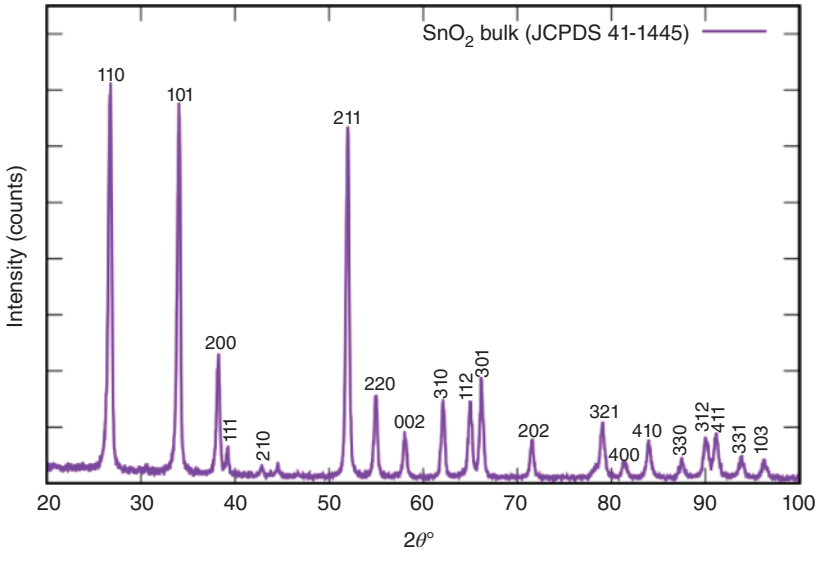

Figure 1.10 XRD pattern of SnO_2 in powder form.

the Debye–Scherrer formula, as given below in Eq. (1.1) [56], where K represents the shape factor with a value of $K = 0.98$ for a cubic unit cell for the spherical crystalline solids [57], β represents the full-width at half-maximum (FWHM), λ is the wavelength of XRD, and θ is the Bragg angle. We have fitted the most pronounced peak (1 1 0) to determine the value of β, by using the Cauchy–Lorentz distribution in the Fityk software. As a result, the crystallite size (D) was found to be around 19 nm. Also, by using Bragg's law $n\lambda = 2d \sin\ \theta$, we calculate the interplanar distance ($d = 3.380$ Å). The lattice parameters have been calculated from XRD parameters for SnO_2 powder. Also, the interplanar spacing formula for a tetragonal unit cell was used as shown in Eq. (1.2) [58].

$$D = \frac{K\lambda}{\beta \cos\ \theta} \tag{1.1}$$

$$\frac{1}{d^2} = \frac{h^2 + k^2}{a^2} + \frac{l^2}{c^2} \tag{1.2}$$

Here d represents the interplanar distance; h, k, l represent the Miller indices, and a, c represent the lattice constants (i.e. $a = b, c$). To calculate the "a" parameter, the second part of the Eq. (1.2) has to vanish. Therefore, we choose the peak that corresponds to (2 0 0) plane with $2\theta = 38.25°$ for powder form. In order to calculate the lattice parameter c, we choose the (0 0 2) plane and its corresponding angle of diffraction $2\theta = 58.1°$ [59, 60] (Table 1.1).

In order to investigate the physical and chemical properties of SnO_2, FTIR and Raman spectroscopies have been exploited to identify and characterize the main vibrational modes of rutile SnO_2, once the sample has been excited with IR and

Table 1.1 Calculation of lattice parameters from XRD of SnO_2 powder.

Sample	2θ°	(*hkl*)	Interplanar distance (*d*) (Å)	Lattice parameter (*a* = *b*) Å	Lattice parameter (*c*) Å
SnO_2 powder	38.25	(2 0 0)	2.351	4.702 4.737[a)]	—
	58.1	(0 0 2)	1.586	—	3.173 3.186[a)]
	2θ°	(*hkl*)	FWHM (2θ°)	Crystallite size (*D*) (nm)	Interplanar distance (*d*) (Å)
	34.04	(1 1 0)	0.424	19.044	3.380

a) Experimental values from A. Schleife et al. [60].

Raman laser sources. The symmetric properties of the tetragonal rutile structure were determined by the 18 vibrational modes at the center of the Brillouin zone, as given by Eq. (1.3).

$$\Gamma = 1A_{1g} + 1A_{2g} + 1B_{1g} + 1B_{2g} + 1E_{1g} + 1A_{2u} + 2B_{1u} + 4E_u \tag{1.3}$$

Four of the vibrational modes are Raman-active, namely the nondegenerate modes, A_{1g}, B_{1g}, B_{2g}, and the doubly degenerate E_g mode. Two modes are IR-active, namely the single A_{2u} mode and the triply degenerate E_u mode. The other two modes are optically inactive modes (i.e. silent modes), namely A_{2g} and B_{1u}, which correspond to the Sn^{4+} and O^{2-} vibrations perpendicular to the *c*-axis and parallel to the *c*-axis, respectively. In the IR-active modes, both Sn^{4+} and O^{2-} ions vibrate along the *c*-axis (i.e. A_{2u} mode) or perpendicular to the *c*-axis (i.e. E_u mode). We have recorded the mid-IR spectra from 400 to 4000 cm^{-1} using an attenuated total reflection (ATR) FTIR accessory with the diamond crystal technique. The spectra were obtained after subtracting the background from the SnO_2 spectra. As illustrated in Figure 1.11, the region from 500 to 700 cm^{-1} is shown for metal oxide vibrations [57, 61]. The IR active mode of SnO_2 powder has been recorded around 467.36 cm^{-1} (see Figure 1.11) that likely corresponds to the A_{2u} (transverse optical [TO]) mode and the 569.37 cm^{-1} feature corresponds to the E_u^3 (TO) vibrational modes both related to the Sn–O stretching vibration [62–64].

In addition to FTIR spectra, the Raman spectra of SnO_2 powder at increasing temperatures were recorded using the DXR™ SmartRaman spectrometer with 780 nm wavelength. The main three Raman-active modes were obtained, namely A_{1g} (634 cm^{-1}), B_{2g} (775 cm^{-1}), and the doubly degenerate E_g (475 cm^{-1}) mode. There was no evidence of the B_{1g} (i.e. between 104 and 125 cm^{-1}) mode in our Raman spectra that should be located around 100 cm^{-1}, as reported in calculations [57, 64, 65]. We have also observed weak peaks at around 502, 546.3, and 695 cm^{-1}, respectively that likely correspond to A_{2u} (TO), B_{1u}, and A_{2u} (longitudinal optical [LO]) modes, respectively. These peaks become more pronounced at higher temperatures (i.e. more than 573 K) and may be due to materials disorder or defects [64, 66]. In the Raman vibrations, the O^{2-} ions are vibrating, whereas Sn^{4+} atoms are stationary, whereby in the nondegenerate modes, A_{1g}, B_{2g}, and B_{1g}, the oxygens vibrate perpendicular to the *c*-axis and in the doubly degenerate E_g vibration mode

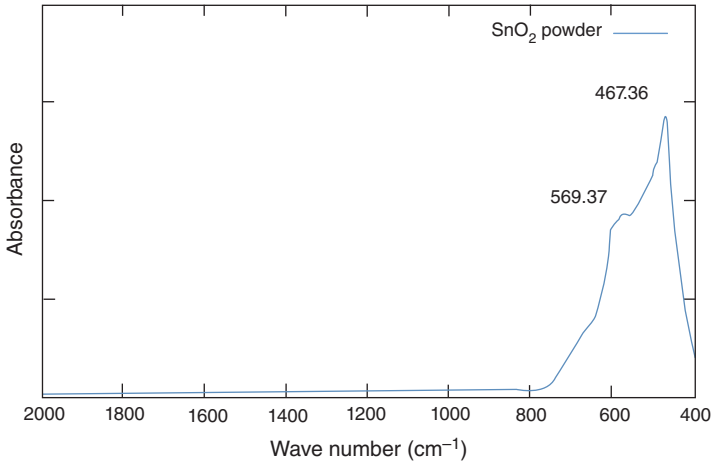

Figure 1.11 FTIR spectrum of SnO_2 powder.

the oxygens vibrate along the *c*-axis [67] (see Figure 1.12) and confirm the tetragonal rutile structure of tin dioxide [68].

The optimal operating temperature is dependent on the sensing material and the type of gases being targeted. Therefore, it is crucial to investigate the optimum temperature for the gas sensors to tie the sensing material to certain target gases in order to enhance their selectivity [34]. In our experimental measurements, we have used the Ventacon^{TM} H4-200 heated cell and varied the temperature of compressed SnO_2 powder in the range 303.15–443.15 K. The overall trend of the behavior of excited Raman modes provided sufficient intensity to analyze and calculate the linewidths and phonon vibration properties, especially for A_{1g} and B_{2g} vibrational modes. In both vibrational modes, A_{1g} and B_{2g}, a measurable shift toward lower wave numbers (i.e. red-shift) as well as linewidth broadenings (i.e. higher FWHM) were observed as the temperature increased. However, the E_g mode exhibited little or no change in wave number and linewidth broadening when compared to the A_{1g} and B_{2g} vibrational modes, perhaps due to molecular orientation effects. These red-shifts toward lower frequency wave numbers confirm the explicit anharmonicity effect in SnO_2 (see Figure 1.13). Pure anharmonicity effects are produced by phonon–phonon interactions at elevated temperatures, which causes phonon frequency shifts and phonon peaks broadenings [64]. As shown in Figure 1.13b,c, B_{2g} exhibits larger anharmonicity than A_{1g}, owing to the difference of O atoms movement toward Sn atoms. In the B_{2g} vibration mode, two of the O atoms are moving toward Sn atoms and the other two O atoms are moving between the Sn atoms in the middle of the vibrational cycle. On the other hand, in the A_{1g} vibration mode, all four O atoms are moving toward one Sn atom during the first half of the moving cycle, and in the other half of the cycle, the four O atoms are moving between two of the Sn atoms, as shown in Figure 1.12b. Such behavior is anticipated to be a result of thermal softening of phonons. When the temperature increases, the phonon entropy increases, since the

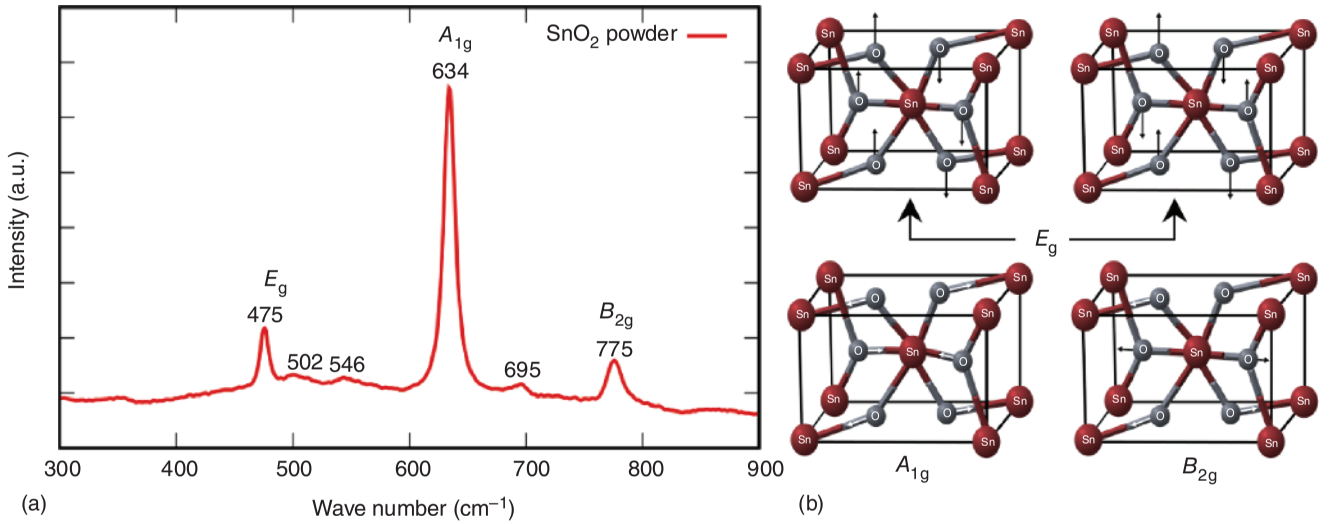

Figure 1.12 (a) Raman vibrational modes of SnO_2 at room temperature; (b) Schematic illustration of Raman-active vibrational modes.

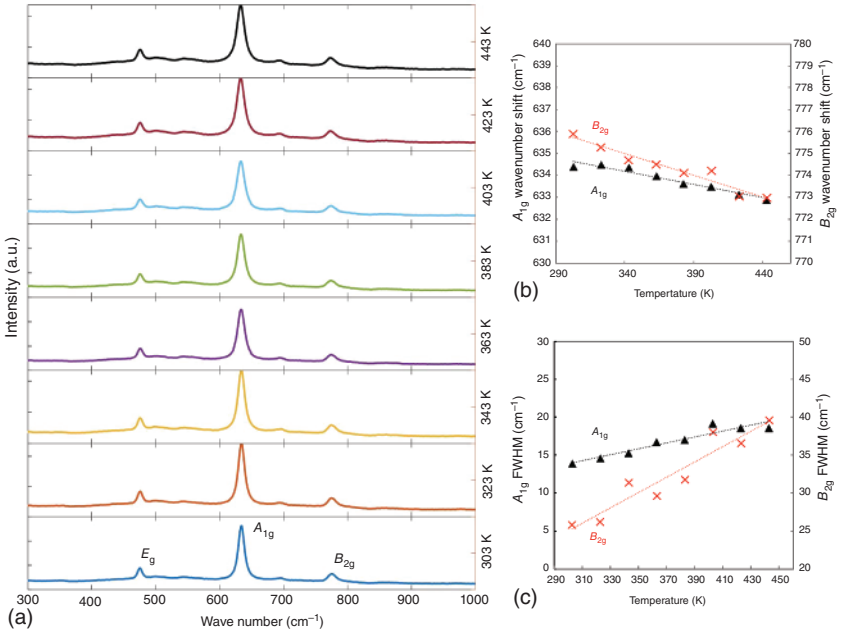

Figure 1.13 (a) Raman spectra of SnO_2 powdered sample at increasing temperature (303–433 K); (b) wave number shifts for A_{1g} and B_{2g} vibration bands with increasing temperature; (c) broadening (FWHMs) of A_{1g} and B_{2g} vibration bands with increasing temperature.

material expands. Therefore, the anharmonic phonon–phonon interaction reduces the lifetime of the phonons [69].

1.3 Graphitic Nanomaterials and Metal Oxide-Based Gas Sensors

1.3.1 Fabrication of Graphitic Nanomaterials-Based Gas Sensors

1.3.1.1 Carbon Nanotube (CNT)-Based Gas Sensors

Previous research studies have extensively reported the fabrication of CNT-based chemiresistive sensors and CNT-based FET sensors for the detection of a variety of gases, such as NH_3, NO_2, O_2, and CO. A study conducted by Valentini et al. [70] in 2003 reported CNTs synthesized by radiofrequency plasma-enhanced chemical vapor deposition (rf-PECVD) technology on Si_3N_4/Si substrates as a chemiresistive gas sensor for sensing NO_2. The electrical properties of CNTs when exposed to NO_2 gas concentrations in the range 10–100 ppb at temperatures in the range 25–250 °C were investigated. It was reported that the electrical resistance decreases on gas exposure with an increase in temperature but reaches its maximum at around 165 °C and therefore concluded that 165 °C should be the operating temperature of a CNT sensor. In addition, their results reported that the CNT film has a fast response time,

fast recovery time, and good selectivity and is highly sensitive to low concentrations of NO_2 at 10 ppb levels with fast response time. It was concluded that temperature is an important tool to consider in improving the sensitivity of the CNT-based gas sensors in the range 3.3–56% at NO_2 concentration of 100 ppb. Li et al. [71] reported the fabrication of a SWCNT-based FET sensor by simple casting SWCNTs on an interdigitated electrode (IDE), using a solution casting process for the detection of NO_2, nitrotoluene and organic vapors at room temperature. The interdigitated electrode was used to ensure optimal gas adsorption on the surface of single-walled carbon nanotubes (SWCNTs) through an effective electrical contact between SWNCNTs and the electrodes. A long recovery time of 10 hours was recorded upon exposure of the SWCNT-based sensor to increasing concentrations of NO_2 from 6 to 100 ppm due to the high bonding energy between NO_2 and SWCNTs. However, a short recovery time of 10 minutes was achieved by using ultraviolet light to displace the adsorbed molecules out of the SWCNT sites. In addition, linear responses of the sensor with respect to increasing concentration of NO_2 and nitrotoluene were observed with the NO_2 detection limit calculated to be 44 ppb and nitrotoluene detection limit calculated to be 262 ppb, respectively.

1.3.1.2 Graphene and Graphene Nanoplatelet (GnP)-Based Gas Sensors

There are different categories of graphene gas sensors, such as chemiresistors, FET, and micro-electromechanical systems (MEMS) gas sensors, which are classified based on their working principles. Chen et al. [72] reported the fabrication of a chemiresistive gas sensor using CVD monolayer graphene on a copper substrate for oxygen detection at room temperature. Raman spectroscopy was carried out to confirm the quality of the CVD-grown graphene and the D, G, and 2D peaks were observed in the Raman spectrum. The detection limit and sensitivity of the sensor were investigated at oxygen concentrations of 1.25%, 2.15%, 3.5%, and 4.7%. An increase in the current of the sensor with increase in concentration of oxygen with a detection limit of 1.25% was reported. In 2020, Srivastava et al. [73] synthesized boron-doped few-layer graphene (BFLGr) nanosheets and pristine few-layer graphene (PFLGr) using a low-pressure chemical vapor deposition (LPCVD) method to fabricate an FET gas-sensing device with Au electrodes for NH_3 detection at room temperature. The current–voltage characteristics of PFLGr and BFLGr-based sensors were investigated in order to study the gas adsorption of NH_3 from −0.5 to 0.5 V, and it was observed that the conductivity of the BFLGr-based gas sensor was 10.25 times lower than the PFLGr-based gas sensor due to the defects present. Their results also indicated that the BFLGr sensor showed a higher response and faster recovery times at increasing concentrations of NH_3 ranging from 16 to 256 ppm (see Figure 1.14), as compared to the PFLGr sensor, implying that the adsorption of NH_3 molecules on the nanosheets is improved upon boron doping. A selectivity test was carried out on the BFLGr-based gas sensor to determine the effects of interfering gases and chemical species by exposing it to CO_2 and H_2 and volatile organic compounds (VOCs) at a concentration of 256 ppm under room temperature conditions. The results showed that the BFLGr sensor is highly selective for NH_3

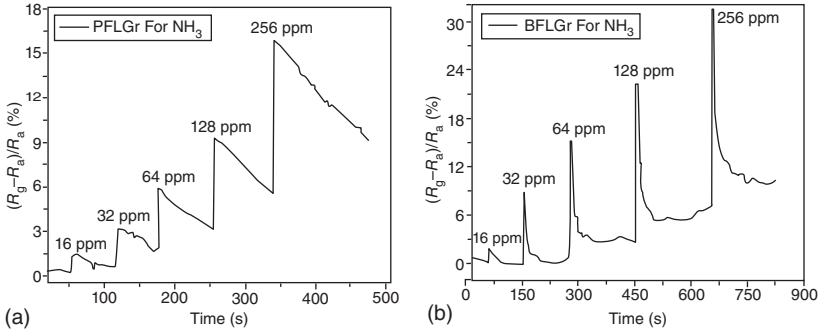

Figure 1.14 Response as a function of time plots for (a) PFLGr and (b) BFLGr for 16–256 ppm concentrations of NH_3. Source: [73] – Published by The Royal Society of Chemistry (RSC) on behalf of the Centre National de la Recherche Scientifique (CNRS) and the RSC. Creative Commons Attribution-NonCommercial 3.0 Unported Licence.

as compared to other interfering gases because of the different adsorption energies of the various gases involved.

In another study conducted by Zhang and Zhang [18] in 2009, an SnO_2/GnP nanocomposite-based gas sensor was fabricated with different mass ratios of SnO_2 and GnPs to sense ethanol vapor. It was reported that the specific surface area of the GnP/SnO_2 nanocomposite, which is 167.01 m^2 g^{-1}, is higher than the specific surface area of SnO_2, which is 119.67 m^2 g^{-1}, as a result of the presence of GnPs. Also, the operating temperature of the GnP/SnO_2-based sensor was found to be 280 °C, and higher sensitivity of the GnP/SnO_2-based sensor with increasing concentrations of ethanol in the range 50–2000 ppm was recorded. The GnP/SnO_2-based sensor showed relatively quicker response and recovery times of 24 and 64 seconds, respectively, as compared to the SnO_2-based gas sensor readings of 81 and 171 seconds response and recovery times, respectively.

1.3.2 Fabrication of Metal Oxide-Based Gas Sensors

Due to the significant rise of hazardous chemical substances in the atmosphere, which can negatively impact the environment for humans, efficient and accurate sensing of harmful gases is urgently needed. Metal oxides have been intensively explored for detecting combustible and toxic gases [74]. Among all harmful chemicals that pollute the environment, carbon monoxide (CO), nitrogen dioxide (NO_2), sulfur dioxide (SO_2), and sulfuric acid (H_2 SO_4) are some of the most prevalent species that can permeate to the ozone layer [34, 75]. Gas detection is crucial in many areas of technology, such as for laboratory air quality, for diagnostic medical sensors, and in agriculture and industry. Indoor air quality is important for human health and safety of building residents where around 90% of city residents spend their time indoors. Besides CO gas detectors, volatile organic chemicals (e.g. formaldehyde and benzene) and NO_2, and ozone (O_3) are considered common pollutants indoors due to the burning of fuels and candles, cleaning products, tobacco consumption, presence of industry, and traffic. Metal oxide-based gas detectors have been examined

as diagnostic devices for specific illnesses, such as lung cancer, diabetes, asthma, halitosis, heart disease, and kidney failure. These diseases are believed to have direct connections with acetone (C_3 H_6O), hydrogen (H_2), ammonia (NH_3), nitrogen monoxide (NO), toluene (C_7 H_8), pentane (C_5 H_{12}), and sulfuric acid (H_2 SO_4) [76].

Presently, semiconductor metal oxides (SMOs) (e.g. WO_3, TiO_2, ZnO, SnO_2, In_2 O_3, etc.) have been investigated widely in gas-sensing applications due to their distinct advantages, such as cost-effectiveness, uncomplicated circuit processing, online monitoring, and compact size [55, 77]. Certain parameters are always considered when evaluating the performance of gas detectors, such as sensitivity, stability, reversibility (recovery time), response time, and selectivity. Sensitivity is defined as the lowest volume density of certain detected target gases at the time of detection. Stability or repeatability is the capability of the sensing material to recover or reproduce parameters over a certain time period. Metal oxide gas detectors with large bandgap energy (E_g) that is higher than 2.5 eV tend to operate decently under high operating temperatures and possess good thermal stability [52]. Reversibility is the time required for a measured sensor's signal to return to its original value after removing the target gases (i.e. around 90% of the original sensing signal). The recovery time depends on the targeted molecular concentration, their adsorption and desorption kinetic temperature, pressure, and the density of the sensed device. Response time is the time required for the sensor's signal to change from an initial reading to a sequential reading, once the sensor is exposed to the target gas (i.e. usually an effective gas sensor detects in seconds to 20 minutes following gas exposure). Selectivity is the capability of the sensing material to detect a certain target gas from a mixture of gases, and it can be calculated by dividing the sensitivity of the gas sensor toward ambient air (Sair) by the sensitivity toward the target gas (S_{gas}) [34, 78].

A variety of gas sensor types have been designed and tested during the past decade depending on the technique and sensing material. Therefore, gas sensors in general are categorized as follows – electrochemical, IR absorption, solid electrolyte, catalytic combustion, and thermal conductive [78]. Metal oxide gas sensors have seen a resurgence in interest and research recently [74]. Nanostructured metal oxides are suitable for various detection mechanisms, such as electrochemical, optical, and electrical sensing methodologies. Electrochemical and optical techniques are the most widely used methods for sensing devices for medical and environmental application. The working principle of electrochemical sensors is based on transferred charge that is caused by oxidation/reduction reaction(s) between the electrode surface and the target gas. Among the metal oxides, SnO_2, ZnO, and TiO_2 are widely deployed to detect and monitor the oxygen level for applications related to medicine, environment, and industry, and for control of car emissions in the ambient air. Most studies on metal oxide gas sensors focus on their resistivity that require high working temperatures, which is considered a disadvantage for the lifetime of the sensor [34]. In a study done by Tan et al., 2017 [79] the researchers developed an optical absorbance gas sensor with Indium-doped ZnO and hydrothermal synthesized ZnO nanorods as sensing materials. This type of optical sensor can operate at room temperatures and can detect carbon monoxide (CO) gas at 10 parts per million level. The sensing technique of such an optical sensor is based on excitement of the

ZnO electrons to the conduction band on UV light illumination, which results in an increase in oxygen adsorption. CO molecules interact with the adsorbed O on the sensing material (ZnO), when the gas sensor is exposed to the CO gas, and thereby enhances the attachment of the CO molecules to the sensing material.

1.3.2.1 Tin Dioxide (SnO_2)-Based Gas Sensors

SnO_2 has been applied in different chemical sensors and transparent conducting electrode applications. It is especially effective at detecting dangerous oxides, such as NO_x, CO, and PbO_2 [74]. The SnO_2 ceramic gas sensor was the first commercial device that was patented by Taguchi in 1968 utilizing SnO_2 and exhibited sensitivity improvements for detecting noble metals and combustible gases [80]. The SnO_2 gas sensor is known to be excellent for detecting VOCs as well, yet it needs improvements in its selectivity for certain gases in presence of other existing compounds [81]. Metal oxide sensors have shown good gas detection results and are cost-effective, user-friendly, and small in size. For many applications, the gas detection tool must have good sensitivity in order to detect a small concentration of a specific gas with high selectivity in the presence of other gases. SnO_2 materials can detect a variety of gaseous compounds, such as hydrogen (H_2), carbon monoxide (CO), and methane (CH_4) [52]. However, SnO_2 sensors have low selectivity due to a large affinity for numerous gases. Besides, SnO_2 gas sensors operate in the high temperature range, typically between 523.15 and 773.15 K [82]. A study conducted by Li et al., in 2019 [83] tested different orientations of SnO_2 films (i.e. (110) and (101)) that was prepared by magnetron sputtering and annealing treatment for sensing. They tested their sensitivity and selectivity of the films toward H_2 and CO and concluded that SnO_2 with (110) orientation (oxygen-rich) has higher sensitivity, response speed, and selectivity for H_2 gas in a mixture of H_2 and CO, as compared to the SnO_2 film with (101) orientation (oxygen-poor) gas sensors. However, these responses were reduced after annealing of SnO_2 (110), as compared to the annealed SnO_2 (101) orientation, which may be due to a change in surface morphology that causes a loss of oxygen and leads to reduction in H_2 sites. SMO gas detectors are mostly used in nanoparticle forms ranging in size between 1 and 100 nm, since certain size-related properties undergo changes due to gas adsorption. Nanomaterials are useful for gas sensing owing to their electrical, optical, magnetic, mechanical, and catalytic features [78]. A study conducted by Ansari et al. showed that by decreasing particle size between 20 and 50 nm by a calcination mechanism, the sensitivity toward low concentration of H_2 gas increases, especially for the particle size of around 20 nm [61]. Furthermore, reducing the grain size between 6 and 16 nm enhances the sensitivity toward H_2S gas, while increasing the grain size to slightly above 16 nm enhances the sensitivity toward H_2 gas.

Metal oxide gas sensors are known to have certain limitations relating to low selectivity. Previous literature has looked at how to enhance the selectivity performance of SnO_2 gas sensors. This section will summarize some of the SnO_2 fabrication methods and their effects on gas-sensing applications. In one study done by Kim et al., in 2018 [84], NiO–SnO_2 thin films were used in gas sensors because of their high sensitivity and selectivity for hazardous gases – nitrogen dioxide (NO_2)

and benzene (C_6H_6). The two composites of nickel(II) oxide (NiO) and SnO_2 were integrated using electrospinning methods. The NiO–SnO_2 composite sensor has a fast response to both NO_2 and C_6H_6 gases due to the presence of significant number of p–n heterojunctions and the affinity of NO_2 for absorbing oxygen. In another study that was done by Kim et al., 2007 [85], a composite of SnO_2 and zinc oxide (ZnO) thin films was used to help enhance selective detection of ethanol (C_2H_5OH) gas. The gas sensor should differentiate ethanol from acetone (C_3H_6O), despite both having similar chemical properties. The formation of the SnO_2–ZnO thin films was done using the so-called "combinatorial solution deposition" technique. The results showed that SnO_2–ZnO composite film sensors exhibited good selectivity for ethanol gas (C_2H_5OH), in comparison to pure SnO_2 and pure ZnO gas sensors.

Zeolites are aluminosilicate crystalline materials that allow small gas particles to pass through and block other larger particles. Therefore, zeolites work as a filter that helps improve the selectivity of semiconductor gas sensors. In an experiment conducted by Sun et al., 2018 [86], SnO_2 gas sensors were coated with MFI-type Zeolites (ZSM-5) to enhance the gas sensor's selectivity toward CO, H_2, and NO_2. The ZSM-5 type is the grain-size layer of zeolites that helps filter out unwanted gas particles. The results in this study showed that the coated SnO_2 gas sensor with ZSM-5 has increased response to the wanted gases and decreased the unwanted gases – for example, acetone preference in case study. In a similar experiment done by Yang et al., 2020 [87], an HZSM-5 zeolite coating was used on SnO_2 to selectively detect methane (CH_4) gas and neglect ethanol and CO as interfering gases. The results showed that the SnO_2 film sensors became selective and sensitive to CH_4. As a result, the zeolite-coated sensors became more resistant to humidity, as compared to the normal SnO_2 gas sensors. Indium oxide (In_2O_3) and SnO_2 composites are used in gas sensors with the aim to enhance the gas sensor's sensing characteristics. The In_2O_3–SnO_2 compound is used to sense molecules such as ethanol (C_2H_5OH) and CO. The In_2O_3–SnO_2 nanocrystals were prepared by the nonaqueous sol–gel technique. The results obtained showed that the increase of tin in the In_2O_3–SnO_2 composite resulted in high sensitivity due to the attachment of oxygen on the surface of the sensing material [88]. The In_2O_3–SnO_2 composite has also been used as a coating on silicon solar cells. In a study conducted by Jain and Kulshreshtha in 1981 [89], the In_2O_3–SnO_2 composite coating was used to help stop the reflection of the solar cell glass and enhance the conductivity of the coating. The In_2O_3–SnO_2 transparent film was made by dc diode sputtering with Ar, N_2, O_2, Xe, and O_2–Ar gas mixture. Such a gas mixture allowed the film to have good adherence and tolerated clearing, polishing, bonding, and heating. The conductive film of In_2O_3–SnO_2 helped decrease the internal series resistance of the solar panel and thereby increased its net power output.

1.4 Conclusions and Future Work

Graphitic nanomaterials have been widely studied for sometime now as potential candidates for gas-sensing applications due to their continued progress in producing advanced gas sensors with high sensitivity and selectivity, fast response

and recovery times, low cost, ease of operation, and room temperature operability. However, there are challenges with the large-scale production of high-quality graphene, which in turn affects the mass production of graphene-based gas sensors and thereby increasing the costs of such sensors. There is also the problem of degradation, non-reproducibility, and instability of graphitic nanomaterials-based gas sensors when fabricated on a large scale. In addition, the cross-sensitivity of graphene when detecting specific gases poses a serious challenge due to its high sensitivity. This implies that graphene-based sensors produce similar responses when exposed to different types of gases and therefore face a challenge relating to their selectivity. Recent advances in fabrication of graphitic nanomaterials-based gas sensors have reported that chemical functionalization with various functional groups, metals and polymers, is a potential tool that can improve the selectivity of such gas sensors. For example, when polymers are incorporated into the structure of graphitic nanomaterials, they are tightly bonded with the target gases and thereby improve their selectivity. It is also important that the fabricated functionalized graphene-based sensors are tested under realistic environmental conditions in the presence of a mixture of gases. Alternately, graphene derivatives, such as GnPs, which can be mass-produced and have the same unique properties as graphene, should also be considered for gas-sensing applications in order to solve the problem of producing graphene-based gas sensors on a large scale.

Metal oxides, akin to graphitic nanomaterials, have been used in a variety of environmental applications and specifically for gas sensing as well. Such oxides have found favor because of their high sensitivity, stability, cost-effectiveness, small size, and easy circuit fabrication and other associated advantages. However, a metal oxide by itself has low selectivity toward specific target gases. Therefore, concerted effort has been exerted toward enhancing the gas selectivity of metal oxide-based sensors by functionalization as discussed earlier. Looking ahead, we are utilizing MD simulation using the LAMMPS software program [51] to study the vibrational properties of pristine and functionalized GnPs and thereby gain better understanding of their Raman characteristics for designing optimal gas sensors. Our focus is on using MD simulation in predicting the lattice dynamics (phonon properties) of GnPs and subsequently generating the phonon dispersion curves. We are initially employing a trilayer graphene model for our GnPs because the individual platelets consist of short stacks of three to six layers of graphene. We plan to extend the MD simulation to four to six layers of graphene, followed by modeling and simulation of bonding target gases (e.g. NO_2, SO_2) to pristine and functionalized GnPs for gas sensors. The LAMMPS [51] modeling and simulation currently being pursued will be followed by COMSOL Multiphysics modeling to simulate and characterize sensing of toxic gases (e.g. NO_2, SO_2) by pristine and functionalized GnPs in an effort to design a prototype gas sensor that can be used for fabrication.

On the tin dioxide front, owing to experimental limitations regarding the available temperature-dependent measurements in our laboratory and incomplete information regarding associated vibrational modes, MD simulation using the LAMMPS software [51] is being used to obtain the phonon dispersion curves of SnO_2 in both bulk and nano forms at elevated temperatures (extending from room temperature

all the way up to 1000 K). Temperature-dependent MD simulations help study the anharmonic effects for SnO_2 bulk and nanoforms and will extend and complement the experimental measurements. Our goal is to determine the phonon dispersion modes using LAMMPS [51] over the entire Brillouin zone. Other studies have shown anharmonicity effects of SnO_2 using first principle calculations, but to the best of our knowledge no comprehensive systematic study has been performed using MD simulation over a wide temperature range (300–1000 K). In order to improve SnO_2 selectivity, researchers have doped, functionalized, and controlled the amount of SnO_2 material to test its ability to selectively detect specific gases and thereby discriminate between say NO_x and CO. The COMSOL Multiphysics software [90] is being utilized to design a prototype SnO_2 gas sensor to detect toxic gases (e.g. NO_x and CO) selectively in trace amounts (at parts per million level).

Acknowledgments

Financial support from the National Science Foundation *REU Site in Physics at Howard University* (NSF Award Nos. PHY 1659224 and PHY 1950379) and *Excellence in Research* (NSF Award No. DMR 2101121), and allocation support from the Extreme Science and Engineering Discovery Environment (XSEDE) Grant Nos. TG-DMR190126 and TG-PHY210066 are gratefully acknowledged.

References

1 Donarelli, M. and Ottaviano, L. (2018). 2D materials for gas sensing applications: a review on graphene oxide, MoS_2, WS_2 and phosphorene. *Sensors* 18 (11): 3638.
2 Yuan, Z., Li, R., Meng, F. et al. (2019). Approaches to enhancing gas sensing properties: a review. *Sensors* 19 (7): 1495.
3 Wu, Z., Chen, X., Zhu, S. et al. (2013). Enhanced sensitivity of ammonia sensor using graphene/polyaniline nanocomposite. *Sensors and Actuators B: Chemical* 178: 485–493.
4 Song, E. and Choi, J.-W. (2013). Conducting polyaniline nanowire and its applications in chemiresistive sensing. *Nanomaterials* 3 (3): 498–523.
5 Pirsa, S. (2017). Chemiresistive gas sensors based on conducting polymers. In: *Handbook of Research on Nanoelectronic Sensor Modeling and Applications* (ed. M.T. Ahmadi, R. Ismail and S. Anwar), 150–180. IGI Global.
6 Tian, W., Liu, X., and Yu, W. (2018). Research progress of gas sensor based on graphene and its derivatives: a review. *Applied Sciences* 8 (7): 1118.
7 Sarf, F. (2020). Metal oxide gas sensors by nanostructures. *Gas Sensors* 1.
8 Ponzoni, A., Baratto, C., Cattabiani, N. et al. (2017). Metal oxide gas sensors, a survey of selectivity issues addressed at the SENSOR Lab, Brescia (Italy). *Sensors* 17 (4): 714.
9 Yang, M., Wang, Y., Dong, L. et al. (2019). Gas sensors based on chemically reduced holey graphene oxide thin films. *Nanoscale Research Letters* 14 (1): 1–8.

10 Zaporotskova, I.V., Boroznina, N.P., Parkhomenko, Y.N., and Kozhitov, L.V. (2016). Carbon nanotubes: sensor properties. A review. *Modern Electronic Materials* 2 (4): 95–105.

11 Alzate-Carvajal, N. and Luican-Mayer, A. (2020). Functionalized graphene surfaces for selective gas sensing. *ACS Omega* 5 (34): 21320–21329.

12 Sahu, P.K., Pandey, R.K., Dwivedi, R. et al. (2020). Polymer/graphene oxide nanocomposite thin film for NO_2 sensor: an in situ investigation of electronic, morphological, structural, and spectroscopic properties. *Scientific Reports* 10 (1): 1–13.

13 Geim, A. and Novoselov, K. (2007). The rise of graphene. *Nature Materials* 6 183–191.

14 Hameed, S. and Bhattarai, P. (2020). Novel nanomaterials for biosensor development. In: *Nanobiosensors: From Design to Applications*, (ed. Aiguo Wu, Waheed S. Khan). 45–72.

15 Raval, B. and Banerjee, I. (2019). Functionalized graphene nanocomposite in gas sensing. In: *Functionalized Graphene Nanocomposites and their Derivatives*, 295–322. Elsevier.

16 Wang, T., Huang, D., Yang, Z. et al. (2016). A review on graphene-based gas/vapor sensors with unique properties and potential applications. *Nano-Micro Letters* 8 (2): 95–119.

17 Iijima, S. (1991). Helical microtubules of graphitic carbon. *Nature* 354 (6348): 56–58.

18 Zhang, W.-D. and Zhang, W.-H. (2009). Carbon nanotubes as active components for gas sensors. *Journal of Sensors* 2009.

19 Wang, Y. and Yeow, J.T.W. (2009). A review of carbon nanotubes-based gas sensors. *Journal of Sensors* 2009. 2.

20 Yoon, H.J., Yang, J.H., Zhou, Z. S.S. et al. (2011). Carbon dioxide gas sensor using a graphene sheet. *Sensors and Actuators B: Chemical* 157 (1): 310–313.

21 Cataldi, P., Athanassiou, A., and Bayer, I.S. (2018). Graphene nanoplatelets-based advanced materials and recent progress in sustainable applications. *Applied Sciences* 8 (9): 1438.

22 Jang, B.Z. and Zhamu, A. (2008). Processing of nanographene platelets (NGPs) and NGP nanocomposites: a review. *Journal of Materials Science* 43 (15): 5092–5101.

23 Casimir, D., Garcia-Sanchez, R., and Misra, P. (2015). Raman spectroscopy and molecular simulation studies of graphitic nanomaterials. In: *Modeling, Characterization, and Production of Nanomaterials*, 179–199. Elsevier.

24 Kumar, M. (2011). Carbon nanotube synthesis and growth mechanism. In: *Carbon Nanotubes-Synthesis, Characterization, Applications*, IntechOpen. 147–170.

25 Mohamed, A.R., Abdullah, A.Z., and Chai, S.-P. (2010). Role of reaction and factors of carbon nanotubes growth in chemical vapour decomposition process using methane-a highlight. *Journal of Nanomaterials* 2010. 1–11. doi:10.1155/2010/395191

26 Bhuyan, M.S.A., Uddin, M.N., Islam, M.M. et al. (2016). Synthesis of graphene. *International Nano Letters* 6 (2): 65–83.

27 Sharma, V., Garg, A., and Sood, S.C. (2015). Graphene synthesis via exfoliation of graphite by ultrasonication. *International Journal of Engineering Trends and Technology (IJETT)* 26: 38–42.

28 Xu, Y., Cao, H., Xue, Y. et al. (2018). Liquid-phase exfoliation of graphene: an overview on exfoliation media, techniques, and challenges. *Nanomaterials* 8 (11): 942.

29 Pirzado, A.A., Le Normand, F., Romero, T. et al. (2019). Few-layer graphene from mechanical exfoliation of graphite-based materials: structure-dependent characteristics. *ChemEngineering* 3 (2): 37.

30 Saeed, M., Alshammari, Y., Majeed, S.A., and Al-Nasrallah, E. (2020). Chemical vapour deposition of graphene-synthesis, characterisation, and applications: a review. *Molecules* 25 (17): 3856.

31 Ding, J.-H., Zhao, H.-R., and Yu, H.-B. (2018). A water-based green approach to large-scale production of aqueous compatible graphene nanoplatelets. *Scientific Reports* 8 (1): 1–8.

32 Guy, O.J. and Walker, K.-A.D. (2016). Graphene functionalization for biosensor applications. In: *Silicon Carbide Biotechnology*, 85–141.

33 Oskam, G. (2006). Metal oxide nanoparticles: synthesis, characterization and application. *Journal of Sol-Gel Science and Technology* 37 (3): 161–164.

34 Viter, R. and Iatsunskyi, I. (2019). Metal oxide nanostructures in sensing. In: *Nanomaterials Design for Sensing Applications*, 41–91. Elsevier.

35 Mohanta, D. and Ahmaruzzaman, M. (2016). Tin oxide nanostructured materials: an overview of recent developments in synthesis, modifications and potential applications. *RSC Advances* 6 (112): 110996–111015.

36 Ginley, D.S. and Perkins, J.D. (2011). Transparent conductors. In: *Handbook of Transparent Conductors*, 1–25. Springer.

37 Karlsson, J. and Roos, A. (2001). Annual energy window performance vs. glazing thermal emittance-the relevance of very low emittance values. *Thin Solid Films* 392 (2): 345–348.

38 Pham, H.P., Nguyen, T.H.Y., Nguyen, A.H.-T. et al. (2020). Effects of substrate temperature on characteristics of the p-type Ag-doped SnO_x thin films prepared by reactive DC magnetron sputtering. *Journal of Photochemistry and Photobiology A: Chemistry* 388: 112157.

39 Zakaryan, H.A. and Aroutiounian, V.M. (2017). Investigation of cobalt doped tin dioxide structure and defects: density functional theory and empirical force fields. *Journal of Contemporary Physics (Armenian Academy of Sciences)* 52 (3): 227–233.

40 Gong, J., Wang, X., Fan, X. et al. (2019). Temperature dependent optical properties of SnO_2 film study by ellipsometry. *Optical Materials Express* 9 (9): 3691–3699.

41 Wang, J., Fan, H.-q., Yu, H.-w., and Wang, X. (2015). Synthesis and optical properties of SnO_2 structures with different morphologies via hydrothermal method. *Journal of Materials Engineering and Performance* 24 (9): 3426–3432.

42 Armstrong, P., Knieke, C., Mackovic, M. et al. (2009). Microstructural evolution during deformation of tin dioxide nanoparticles in a comminution process. *Acta Materialia* 57 (10): 3060–3071.

43 Oviedo, J. and Gillan, M.J. (2000). Energetics and structure of stoichiometric SnO_2 surfaces studied by first-principles calculations. *Surface Science* 463 (2): 93–101.

44 Misra, P., Casimir, D., and Garcia-Sanchez, R. (2014).Raman spectroscopy and molecular dynamics simulation studies of carbon nanotubes. In: *Physics of Semiconductor Devices*, 507–510. Springer.

45 Botti, S., Rufoloni, A., Rindzevicius, T., and Schmidt, M.S. (2018). Surface-enhanced Raman spectroscopy characterization of pristine and functionalized carbon nanotubes and graphene. *Raman Spectroscopy* 203.

46 Misra, A., Tyagi, P.K., Rai, P., and Misra, D.S. (2007). FTIR spectroscopy of multiwalled carbon nanotubes: a simple approach to study the nitrogen doping. *Journal of Nanoscience and Nanotechnology* 7 (6): 1820–1823.

47 Casimir, D., Alghamdi, H., Ahmed, I.Y. et al. (2019). Raman spectroscopy of graphene, graphite and graphene nanoplatelets. In: *2D Materials*. IntechOpen.

48 Tuinstra, F. and Koenig, J.L. (1970). Raman spectrum of graphite. *The Journal of Chemical Physics* 53 (3): 1126–1130.

49 Thema, F.T., Moloto, M.J., Dikio, E.D. et al. (2013). Synthesis and characterization of graphene thin films by chemical reduction of exfoliated and intercalated graphite oxide. *Journal of Chemistry* 2013. 4.

50 Farinre, O., Alghamdi, H., and Misra, P. (2021). Spectroscopic characterization and molecular dynamics simulation of tin dioxide, pristine and functionalized graphene nanoplatelets. In: *International Conference on Computational & Experimental Engineering and Sciences*, 29–43. Springer.

51 Kong, L.T. (2011). Phonon dispersion measured directly from molecular dynamics simulations. *Computer Physics Communications* 182: 2201–2207. http://lammps.sandia.gov.

52 Korotcenkov, G., Brinzari, V., and Ham, M.H. (2018). Materials acceptable for gas sensor design: advantages and limitations. In: *Key Engineering Materials*, (ed. Vladimir Khovaylo, Ghenadii Korotcenkov). vol. 780, 80–89. Trans Tech Publications.

53 Zhou, J.X., Zhang, M.S., Hong, J.M., and Yin, Z. (2006). Raman spectroscopic and photoluminescence study of single-crystalline SnO_2 nanowires. *Solid State Communications* 138 (5): 242–246.

54 Alghamdi, H., Concepcion, B., Baliga, S., and Misra, P. (2020). Synthesis, spectroscopic characterization and applications of tin dioxide. In: *Contemporary Nanomaterials in Material Engineering Applications*, 285–318. Springer.

55 Batzill, M. (2006). Surface science studies of gas sensing materials: SnO_2. *Sensors* 6 (10): 1345–1366.

56 Henry, J., Mohanraj, K., Sivakumar, G., and Umamaheswari, S. (2015). Electrochemical and fluorescence properties of SnO_2 thin films and its antibacterial activity. *Spectrochimica Acta Part A: Molecular and Biomolecular Spectroscopy* 143: 172–178.

57 Ferreira, C.S., Santos, P.L., Bonacin, J.A. et al. (2015). Rice husk reuse in the preparation of SnO_2/SiO_2 nanocomposite. *Materials Research* 18 (3): 639–643.

58 Surbhi, S. and Kumar, S. (2014). Studies on structural parameters of ZrO_2–SnO_2 binary system. In: *Physics of Semiconductor Devices*, 717–719. Springer.

59 Sharma, A., Prakash, D., and Verma, K.D. (2009). Optical characterization of hydrothermally grown SnO_2 nanocrystals. *Journal of Optoelectronics and Advanced Materials* 3: 331–337.

60 Schleife, A., Varley, J.B., Fuchs, F. et al. (2011). Tin dioxide from first principles: quasiparticle electronic states and optical properties. *Physical Review B* 83 (3): 035116.

61 Ansari, S.G., Fouad, H., Shin, H.-S., and Ansari, Z.A. (2015). Electrochemical enzyme-less urea sensor based on nano-tin oxide synthesized by hydrothermal technique. *Chemico-Biological Interactions* 242: 45–49.

62 Mahadik, D.B., Lee, Y.K., Park, C.-S. et al. (2015). Effect of water ethanol solvents mixture on textural and gas sensing properties of tin oxide prepared using epoxide-assisted sol–gel process and dried at ambient pressure. *Solid State Sciences* 50: 1–8.

63 Amalric-Popescu, D. and Bozon-Verduraz, F. (2001). Infrared studies on SnO_2 and Pd/SnO_2. *Catalysis Today* 70 (1–3): 139–154.

64 Lan, T., Li, C.W., and Fultz, B. (2012). Phonon anharmonicity of rutile SnO_2 studied by Raman spectrometry and first principles calculations of the kinematics of phonon–phonon interactions. *Physical Review B* 86 (13): 134302.

65 Dieguez, A., Romano-Rodrıguez, A., Vila, A., and Morante, J.R. (2001). The complete Raman spectrum of nanometric SnO_2 particles. *Journal of Applied Physics* 90 (3): 1550–1557.

66 Bonu, V., Das, A., Sivadasan, A.K. et al. (2015). Invoking forbidden modes in SnO_2 nanoparticles using tip enhanced Raman spectroscopy. *Journal of Raman Spectroscopy* 46 (11): 1037–1040.

67 Wong, P.T.T. (1975). Pressure and temperature dependences of the Raman-active phonons in dichlorobis(pyridine)zinc(II) crystal. *The Journal of Chemical Physics* 63 (12): 5108–5115.

68 Guan, X., Wang, Y., Luo, P. et al. (2019). Incorporating n atoms into SnO_2 nanostructure as an approach to enhance gas sensing property for acetone. *Nanomaterials* 9 (3): 445.

69 Kim, D.S. (2018). Silicon revisited: understanding pure phonon anharmonicity and the effects on thermophysical properties. PhD thesis. California Institute of Technology.

70 Valentini, L., Armentano, I., Kenny, J.M. et al. (2003). Sensors for sub-ppm NO_2 gas detection based on carbon nanotube thin films. *Applied Physics Letters* 82 (6): 961–963.

71 Li, J., Lu, Y., Ye, Q. et al. (2003). Carbon nanotube sensors for gas and organic vapor detection. *Nano Letters* 3 (7): 929–933.

72 Chen, C.W., Hung, S.C., Yang, M.D. et al. (2011). Oxygen sensors made by monolayer graphene under room temperature. *Applied Physics Letters* 99 (24): 243502.

73 Srivastava, S., Jain, S.K., Gupta, G. et al. (2020). Boron-doped few-layer graphene nanosheet gas sensor for enhanced ammonia sensing at room temperature. *RSC Advances* 10 (2): 1007–1014.

74 Mandal, S., Natarajan, S., Tamilselvi, A., and Mayadevi, S. (2016). Photocatalytic and antimicrobial activities of zinc ferrite nanoparticles synthesized through soft chemical route: a magnetically recyclable catalyst for water/wastewater treatment. *Journal of Environmental Chemical Engineering* 4 (3): 2706–2712.

75 Nasiri, N. and Clarke, C. (2019). Nanostructured gas sensors for medical and health applications: low to high dimensional materials. *Biosensors* 9 (1): 43.

76 Deng, Y. (2019). Applications of semiconducting metal oxides gas sensors. In: *Semiconducting Metal Oxides for Gas Sensing*, 195–241. SpringerLink.

77 Das, S. and Akhtar, J. (2014). Comparative study on Temperature Coefficient of Resistance (TCR) of the E-beam and sputter deposited nichrome thin film for precise temperature control of microheater for mems gas sensor. In: *Physics of Semiconductor Devices*, 495–497. Springer.

78 Dey, A. (2018). Semiconductor metal oxide gas sensors: a review. *Materials Science and Engineering B* 229: 206–217.

79 Tan, C.H., Tan, S.T., Lee, H.B. et al. (2017). Automated room temperature optical absorbance CO sensor based on In-doped ZnO nanorod. *Sensors and Actuators B: Chemical* 248: 140–152.

80 Ihokura, K. and Watson, J. (2017). *The Stannic Oxide Gas Sensor Principles and Applications*. CRC press.

81 Choi, P.G., Izu, N., Shirahata, N., and Masuda, Y. (2019). SnO_2 nanosheets for selective alkene gas sensing. *ACS Applied Nano Materials* 2 (4): 1820–1827.

82 Hijazi, M., Stambouli, V., Rieu, M. et al. (2017). Sensitive and selective ammonia gas sensor based on molecularly modified SnO_2. In: *Multidisciplinary Digital Publishing Institute Proceedings*, vol. 1, 399.

83 Li, R., Zhou, Y., Sun, M. et al. (2019). Gas sensing selectivity of oxygen-regulated SnO_2 films with different microstructure and texture. *Journal of Materials Science and Technology* 35 (10): 2232–2237.

84 Kim, J.-H., Lee, J.-H., Mirzaei, A. et al. (2018). SnO_2 (n)-NiO (p) composite nanowebs: gas sensing properties and sensing mechanisms. *Sensors and Actuators B: Chemical* 258: 204–214.

85 Kim, K.-W., Cho, P.-S., Kim, S.-J. et al. (2007). The selective detection of C_2H_5OH using SnO_2–ZNO thin film gas sensors prepared by combinatorial solution deposition. *Sensors and Actuators B: Chemical* 123 (1): 318–324.

86 Sun, Y., Wang, J., Li, X. et al. (2018). The effect of zeolite composition and grain size on gas sensing properties of SnO_2/zeolite sensor. *Sensors* 18 (2): 390.

87 Yang, B., Zhang, Z., Tian, C. et al. (2020). Selective detection of methane by HZSM-5 zeolite/Pd-SnO_2 gas sensors. *Sensors and Actuators B: Chemical* 321: 128567.

88 Neri, G., Bonavita, A., Micali, G. et al. (2008). Effect of the chemical composition on the sensing properties of In_2O_3–SnO_2 nanoparticles synthesized by a non-aqueous method. *Sensors and Actuators B: Chemical* 130 (1): 222–230.

89 Jain, V.K. and Kulshreshtha, A.P. (1981). Indium-tin-oxide transparent conducting coatings on silicon solar cells and their "figure of merit". *Solar Energy Materials* 4 (2): 151–158.

90 COMSOL Multiphysics (1998). Introduction to COMSOL multiphysics®. *COMSOL Multiphysics*, Burlington, MA. accessed February 9 2018.